Advanced single-slice rebinning in cone-beam spiral CT: Theoretical considerations and medical applications

Article *in* Proceedings of SPIE - The International Society for Optical Engineering · June 2000

Impact Factor: 0.2 · DOI: 10.1117/12.387710

Advanced single–slice rebinning in cone–beam spiral CT: Theoretical considerations and medical applications

Marc Kachelrieß[a], Stefan Schaller[b] and Willi A. Kalender[a]

[a]Institute of Medical Physics, Krankenhausstr. 12, 91054 Erlangen, Germany
[b]Siemens AG, Medical Engineering Group, CT division,
Siemensstr. 1, 91301 Forchheim, Germany

ABSTRACT

The advanced single–slice rebinning algorithm (ASSR) is a highly accurate and efficient approximative algorithm for cone–beam spiral CT that a) yields high image quality even at large cone angles, b) makes use of available 2D backprojection algorithms/hardware and c) allows for sequential data processing. It uses virtual R–planes (reconstruction planes) that are tilted to optimally fit 180° spiral segments. Along these R–planes data of a virtual 2D parallel scanner are synthesized via rebinning from the measured spiral cone–beam data. Reconstruction with 2D filtered backprojection yields the object cross-section in world coordinates $(x, y, z(x, y))$ which is resampled to Cartesian coordinates (x, y, z) by z–filtering. Geometrical misalignments as well as any arbitrary detector geometry can be easily incorporated in the ASSR algorithm.

ASSR, unlike other approximate algorithms, does not show severe cone–beam artifacts when going to larger cone angles. Even for scanners with a high number of detector rows, e.g. 64 rows, a high and isotropic z–resolution is achieved. In–plane resolution is determined by the 2D reconstruction filters which can be chosen as in 2D CT. Even in the case of only $M = 4$ or $M = 8$ simultaneously measured slices, ASSR may outperform standard z–interpolation algorithms such as 180°MFI. Due to its high efficiency and high image quality ASSR has the potential to be used for medical cone–beam CT.

Keywords: Computed tomography (CT), Multi–slice Spiral CT, Multi–row detector systems, Cone–beam detector systems, 3D reconstruction

1. INTRODUCTION

Future developments in medical CT are aiming at increasing spatial resolution and at improving the volume scanning capability of the CT scanners.[1] The latest step towards this goal was the introduction of multi–slice CT scanners in 1998. The number of simultaneously acquired slices nowadays is typically $M = 4$. However, there is a strong desire to further improve the volume coverage speed and/or the z–resolution of the scanners. This can be achieved only by increasing the number of detector rows. Increasing the number of detector rows, however, will lead to the problem of cone–beam reconstruction since the acquired data cannot be considered as being approximately perpendicular to the z–axis anymore.

Quite a few cone–beam reconstruction algorithms have been proposed in the past. They can be divided into exact cone–beam algorithms[2–5] and approximate cone–beam algorithms.[6–10] However, all of them suffer from certain drawbacks which will not allow their usage for medical CT. For example the exact algorithms are computationally too demanding and consequently the reconstruction time is too high to be used in a medical environment. Moreover, data truncation, solved by data combination, and the long object problem, theoretically solvable as well, introduce new artifacts due to the inherent discrete nature of the measured data. The approximate approaches, in contrast, are computationally very efficient. However, with increasing cone angle the artifact content is increased drastically and, even for a low number M of simultaneously measured slices (e.g. $M = 16$, assuming the typical geometry of a medical CT scanner), the artifact level of the known approximate algorithms becomes unacceptable for medical use.

Further author information:
(Send correspondence and reprint requests to Marc Kachelrieß)
Marc Kachelrieß: marc.kachelriess@imp.uni-erlangen.de
Stefan Schaller: stefan.schaller@med.siemens.de
Willi A. Kalender: willi.kalender@imp.uni-erlangen.de

Stimulated by the single–slice rebinning algorithm[11] (SSR) we consider a new approach here: the advanced single–slice rebinning ASSR. The difference to the original single–slice rebinning is that ASSR uses tilted reconstruction planes that are optimized to fit the spiral trajectory within an angular range of $2\pi f$ with $\frac{1}{2} \le f \le 1$.

ASSR has been derived in its full length in a previous paper.[12] The current paper will briefly state the results needed to perform the reconstruction. As the gold standard for comparison we use simulated data using single–slice spiral CT geometry at a pitch value of $p = d/MS = 1.5$ where M is the number of simultaneously measured slices and S is the collimated slice width. These gold standard data are reconstructed using 180°LI (Linear Interpolation).[1] However, comparisons of ASSR are not only performed to the gold standard 180°LI but also to the multi–slice algorithms 180°MFI (Multi–slice Filtered Interpolation)[1] for scanners with $M = 4$ and $M = 8$ slices.

The simulations of our virtual thorax phantom are presented for a large number of scan geometries, i.e. varying number M of simultaneously measured slices. The phantom definition can be found in the world–wide phantom data base at `http://www.imp.uni-erlangen.de/phantoms`. It is designed to completely fill a field of measurement (FOM) of 500 mm diameter. The simulated slice thickness is $S = 1$ mm and the table increments simulated are $d \in \{1.5, 6, 12, 16, 32, 64, 96\}$ mm. The number M of simultaneous measured slices can be calculated from the overall constant pitch value $p = 1.5$ using $M = d/pS$. The in–plane scanner geometry was chosen to be equivalent to the SOMATOM Plus 4 Volume Zoom (Siemens, Medical Systems, Erlangen, Germany), i.e. the radius of the FOM is $R_{\mathrm{M}} = 250$ mm, the distance from the isocenter to the focal spot is $R_{\mathrm{F}} = 570$ mm and thus the fan angle is $\Phi = 52°$.

2. NOMENCLATURE

This section presents an alphabetically sorted summary of the variables and notations used in the paper. Most of them will be introduced in the text as well.

The ASSR algorithm will be stated in flat detector coordinates (u, v), for convenience. The transformation from flat detector coordinates to other geometries, such as the cylindrical detector used in our simulations, is straightforward and will be omitted here.

$x \vee y$	maximum function, $x \vee y = \max(x, y)$
$x \wedge y$	minimum function, $x \wedge y = \min(x, y)$
α	projection angle, $\alpha \in \mathbb{R}$
α^*	attachment angle of the tilted planes. A reconstruction plane centered about α_{R} will be attached to the spiral trajectory at $\alpha = \alpha_{\mathrm{R}}$ and $\alpha = \alpha_{\mathrm{R}} \pm \alpha^*$
α'	focus position relative to the reconstruction position α_{R}, $\alpha' = \alpha - \alpha_{\mathrm{R}}$
α'_{L}	focus position for the longitudinal approximation to use in rebinning when the rebinned ray has the parameters ϑ' and ξ'
α_{R}	projection angle about which the reconstruction is centered
d	table increment per 360° rotation, $d \in \mathbb{R}$
D	detector plane
$\cos\varepsilon$	length correction factor to account for the angle ε between the measured ray and the virtual ray used for reconstruction, see section 3.1
$\boldsymbol{e}(\alpha)$	elliptical trajectory of the virtual focus. The ellipse is tilted by the angle γ to optimally match the given focus trajectory $\boldsymbol{s}(\alpha)$ in the interval $\alpha \in [\alpha_{\mathrm{R}} - f\pi, \alpha_{\mathrm{R}} + f\pi)$
f	fraction of 360° (in parallel geometry) to be used for reconstruction. Projection angles ϑ within $[-f\pi, f\pi)$ will be used considering projections rebinned to parallel geometry. $f = \frac{1}{2}$ is a half scan reconstruction, $f > \frac{1}{2}$ means overscan data to reduce interpolation artifacts

$\varPhi$	fan angle, $\varPhi = 2\sin^{-1}(R_\mathrm{M}/R_\mathrm{F})$
γ	tilt angle of the reconstruction plane R measured with respect to the x–y–plane
$\boldsymbol{o}'$	origin of the primed coordinate systems
p	pitch value. It is defined as the table increment d divided by the intersection length of the collimated cone–beam and the z–axis: $p = d/MS$
$p(\alpha, u, v)$	measured projection data at (α, u, v)
$p(\vartheta, \xi)$	rebinned projection data
R	reconstruction plane, $\mathrm{R} \supset \boldsymbol{e}(\mathbb{R})$, see equation (2)
R_D	distance from detector to center of rotation (z–axis), in our case 435 mm
R_F	distance from focus to center of rotation (z–axis), in our case 570 mm
R_M	radius of the field of measurement (FOM), in our case 250 mm
S	slice thickness, as projected onto the axis of rotation = physical beam width, i.e. z–range over which a physical averaging is performed during the measurement process
$\boldsymbol{s}(\alpha)$	spiral focus trajectory
ϑ, ξ	beam parameters in parallel geometry
u, v	detector coordinates
u_F, v_F	detector coordinates for the fan–beam based approximation
$z(x, y)$	z–coordinate of a point $\boldsymbol{r} \in \mathrm{R}$ as a function of its x– and y–coordinates
z_R	reconstruction position of the final (non tilted) image
Δz_mean	average deviation of the focus from the reconstruction ellipse
(C/W)	window setting of the reconstructed images in HU. C is the window center, W the window width

We will denote the respective reconstruction algorithms and the simulated table increment by appending the table increment value to the algorithm's name, for convenience. E.g. ASSR96 means that the reconstruction was performed using the ASSR algorithm and the scanner used was the one with $d = 96$ mm. Most comparisons are done to the standard single–slice algorithm 180°LI using data simulated with a table increment of $d = 1.5$ mm which is consequently denoted as 180°LI1.5.

3. RECONSTRUCTION

For our considerations we assume the spiral focus trajectory to be as follows:

$$\boldsymbol{s}(\alpha) = \begin{pmatrix} R_\mathrm{F}\sin\alpha \\ -R_\mathrm{F}\cos\alpha \\ d\,\alpha/2\pi \end{pmatrix}; \quad \alpha \in \mathbb{R} \; .$$

Thereby, d denotes the table increment per rotation and R_F is the distance of the focal spot to the center of rotation. The parameter α is used to denote the rotational angle of the gantry and since we are dealing with a spiral scan we can use α to determine the z–position of the focal spot as well.

Assuming a planar detector geometry we use the following parameter representation

$$\mathrm{D}: \boldsymbol{r}(u, v) = \begin{pmatrix} -R_\mathrm{D}\sin\alpha \\ R_\mathrm{D}\cos\alpha \\ d\,\alpha/2\pi \end{pmatrix} + u\begin{pmatrix} \cos\alpha \\ \sin\alpha \\ 0 \end{pmatrix} + v\begin{pmatrix} 0 \\ 0 \\ 1 \end{pmatrix}$$

and the normal representation

$$\mathrm{D}: x\sin\alpha - y\cos\alpha + R_\mathrm{D} = 0 \; .$$

The origin of the detector coordinates ($u = 0, v = 0$) is the orthogonal projection of the vertex $\boldsymbol{s}(\alpha)$ onto the detector plane. The parameter R_{D} gives the distance of the detector to the center of rotation. The distance of the focal spot to the detector plane is given by $R_{\mathrm{D}} + R_{\mathrm{F}}$.

The procedure to be described will do a rebinning from the measured attenuation data $p(\alpha, u, v)$ to parallel data $p(\vartheta, \xi)$. The value ϑ describes the angle of the ray with respect to the y–axis and ξ describes its signed distance to the isocenter. Each single–slice reconstruction will be centered about a certain angle α_{R} and thus the range of ϑ playing a role for the reconstruction will be $\vartheta \in [\alpha_{\mathrm{R}} - f\pi, \alpha_{\mathrm{R}} + f\pi)$. $f \geq \frac{1}{2}$ is a parameter to adjust the degree of overscan used for the reconstruction. The minimal value $f = \frac{1}{2}$ corresponds to using exactly 180° rebinned parallel data. However, some overscan views might be necessary to reduce artifacts in the images and hence we have introduced the parameter f (the images shown in this paper all use $f = 52\%$). Of course, the α–range required for rebinning will be one fan–angle larger than the ϑ–range needed for reconstruction.

The ASSR algorithm aims at predicting the optimal tilted reconstruction plane and thus the optimal elliptical virtual focus trajectory

$$\boldsymbol{e}(\alpha) = \boldsymbol{o}' + R_{\mathrm{F}} \begin{pmatrix} \sin\alpha \\ -\cos\alpha \\ \tan\gamma\,\sin(\alpha - \alpha_{\mathrm{R}}) \end{pmatrix} \qquad \text{with} \qquad \boldsymbol{o}' = \begin{pmatrix} 0 \\ 0 \\ d\frac{\alpha_{\mathrm{R}}}{2\pi} \end{pmatrix}$$

such that the physical focus position $\boldsymbol{s}(\alpha)$ deviates only minimally from the virtual focus position $\boldsymbol{e}(\alpha)$ for all $\alpha \in [\alpha_{\mathrm{R}} - f\pi, \alpha_{\mathrm{R}} + f\pi)$. The reconstruction plane R, defined by $\boldsymbol{e}(\mathbb{R}) \subset \mathrm{R}$, can easily be derived from the generalized ellipse formula:

$$\mathrm{R}: \; x\cos\alpha_{\mathrm{R}}\,\tan\gamma + y\sin\alpha_{\mathrm{R}}\,\tan\gamma - z + d\frac{\alpha_{\mathrm{R}}}{2\pi} = 0\,. \tag{2}$$

The tilt angle γ is the angle between the reconstruction plane R and the transaxial x–y–plane, $\tan\gamma$ thus gives the slope of R. Regarding the mean absolute z–deviation

$$\Delta z_{\mathrm{mean}} = \frac{1}{2\pi f}\int\limits_{\alpha_{\mathrm{R}}-f\pi}^{\alpha_{\mathrm{R}}+f\pi} d\alpha\,|\boldsymbol{e}(\alpha) - \boldsymbol{s}(\alpha)| = \frac{1}{2\pi f}\int\limits_{-f\pi}^{f\pi} d\alpha'\,|R_{\mathrm{F}}\tan\gamma\,\sin\alpha' - d\frac{\alpha'}{2\pi}| = \frac{1}{\pi f}\int\limits_{0}^{f\pi} d\alpha'\,|R_{\mathrm{F}}\tan\gamma\,\sin\alpha' - d\frac{\alpha'}{2\pi}|$$

with $\alpha' = \alpha - \alpha_{\mathrm{R}}$ one finds

$$\Delta z_{\mathrm{mean}} = \frac{d}{2\pi}\frac{1}{f\pi}\begin{cases} \frac{2\pi}{d}R_{\mathrm{F}}\tan\gamma\,(1 + \cos f\pi - 2\cos\alpha^*) + \frac{1}{2}f^2\pi^2 - {\alpha^*}^2 & \text{for} \quad 1 \leq \frac{2\pi}{d}R_{\mathrm{F}}\tan\gamma \leq \frac{f\pi}{\sin f\pi} \\ \left|\frac{2\pi}{d}R_{\mathrm{F}}\tan\gamma\,(\cos f\pi - 1) + \frac{1}{2}f^2\pi^2\right| & \text{elsewhere} \end{cases} \tag{3}$$

where $\alpha^* \in [0, \pi)$ is given by

$$\frac{2\pi}{d}R_{\mathrm{F}}\tan\gamma = \frac{\alpha^*}{\sin\alpha^*}\,.$$

The new angle α^* is called the attachment angle since it gives the points of intersection of the plane R and the virtual elliptical trajectory $\boldsymbol{e}(\mathbb{R})$. To be more precise, the spiral scan trajectory and the ellipse will intersect at α_{R} and $\alpha_{\mathrm{R}} \pm \alpha^*$.

Minimizing Δz_{mean} with respect to the tilt angle γ we find the minimal value

$$\Delta z_{\mathrm{mean}} = d\frac{f^2\pi^2 - 2{\alpha^*}^2}{4f\pi^2}$$

to occur for

$$\cos\alpha^* = \tfrac{1}{2}(1 + \cos f\pi).$$

Using $f = \frac{1}{2}$ yields the result $\alpha^* = 60°$ which is quite descriptive since the attachment positions 0° and ±60° uniformly divide the reconstruction interval ranging from −90° to 90° (α_{R} was set to zero for this example). In this case a mean z deviation as low as $\Delta z_{\mathrm{mean}} = d/72$ is achieved, i.e. the physical and virtual trajectories differ by 1.4% of the table feed on average.

The behaviour of Δz_{mean} as a function of $\frac{2\pi}{d}R_{\text{F}}\tan\gamma$ is shown in figure 1. From this figure it becomes clear that the optimal region lies around $\alpha^* = 60°$ and one should stay within about $\pm 10°$ from this optimum in order not to increase the mean z–deviation significantly.

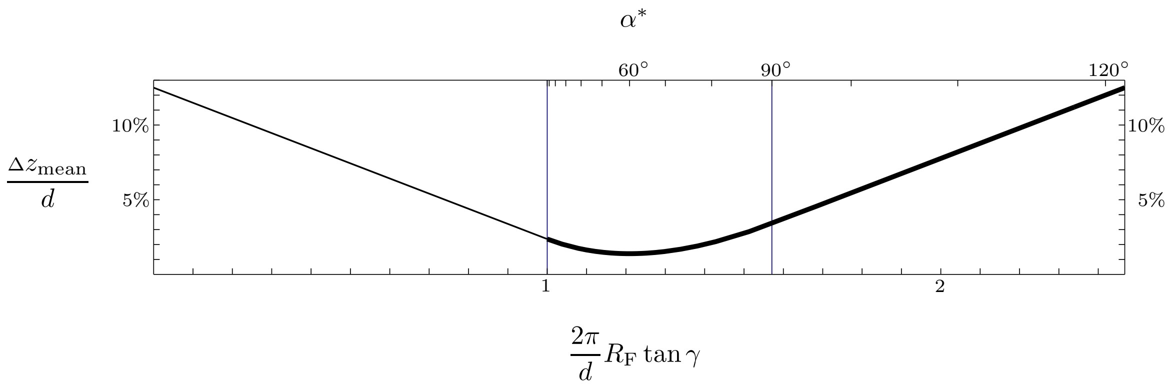

Figure 1. Plot of the relative mean deviation $\Delta z_{\text{mean}}/d$ as a function of $\frac{2\pi}{d}R_{\text{F}}\tan\gamma$ for $f = \frac{1}{2}$. The upper axis additionally shows the attachment angle α^* in steps of 10°. The minimal z–deviation occurs for $\alpha^* = 60°$ which is equivalent to $\frac{2\pi}{d}R_{\text{F}}\tan\gamma = 2\pi/3\sqrt{3} \approx 1.2092$. The thick part of the graph depicts those values for which the case of three intersections is met and thus α^* is defined. The region between the two vertical grid lines corresponds to the first case of equation (3) whereas the regions on the left and right side correspond to the "elswhere" part of (3). It must be mentioned that although the graph appears to be symmetric with respect to its minimum this actually is not the case.

3.1. Rebinning

The rebinning procedure to be performed is a fan–based longitudinal optimization.[12] For each ray (ϑ, ξ) to be rebinned into parallel geometry the optimal focus position α'_{L} (longitudinal approximation) and the optimal detector coordinates u_{F} and v_{F} (fan–based ray selection) are to be selected as follows:

$$\begin{aligned}
\alpha'_{\text{L}}(\vartheta,\xi) &:= \vartheta + \sin^{-1}\frac{\xi}{R_{\text{F}}} && \text{focus position} \\
u_{\text{F}}(\vartheta,\xi,\alpha') &:= \frac{R_{\text{D}}+R_{\text{F}}}{R_{\text{F}}}\frac{\xi}{\cos(\alpha'-\vartheta)} && \text{transaxial detector coordinate} \\
v_{\text{F}}(\vartheta,\xi,\alpha') &:= \frac{R_{\text{D}}+R_{\text{F}}}{R_{\text{F}}}\left(\frac{\xi\cos\alpha'\,\tan\gamma}{\cos(\alpha'-\vartheta)} - d\frac{\alpha'}{2\pi}\right) && \text{axial detector coordinate.}
\end{aligned} \tag{4}$$

The rebinned parallel rawdata $p(\vartheta, \xi)$ must be multiplied with the length correction factor

$$\cos\varepsilon(\alpha',\vartheta,u,v) = \frac{u\sin(\alpha'-\vartheta)\cos\gamma + (R_{\text{D}}+R_{\text{F}})\cos(\alpha'-\vartheta)\cos\gamma - v\sin\vartheta\,\sin\gamma}{\sqrt{u^2+v^2+(R_{\text{D}}+R_{\text{F}})^2}\sqrt{\sin^2\vartheta+\cos^2\gamma\,\cos^2\vartheta}}$$

to compensate for the angle between the measured rays and the virtual rays (that lie in the R–plane) that are used for the reconstruction. Reconstructing these data, using filtered backprojection for example, would yield the tilted image on a tilted Cartesian grid corresponding to the plane R. Bringing it to Cartesian world coordinates would require an additional interpolation step from discrete points of the tilted image to the discrete voxel locations of the world's Cartesian system. However, it has been shown that this step can be avoided by multiplying the data with the correction factor $\cos\gamma/\sqrt{\sin^2\vartheta+\cos^2\gamma\,\cos^2\vartheta}$. To summarize, for each $\vartheta \in [\alpha_{\text{R}} - f\pi, \alpha_{\text{R}} + f\pi)$ and each $\xi \in [-\frac{1}{2}R_{\text{M}}, \frac{1}{2}R_{\text{M}}]$ we use the following rebinning equation

$$p(\vartheta,\xi) := \frac{\cos\gamma\,\cos\varepsilon(\alpha'_{\text{L}},\vartheta,u_{\text{F}},v_{\text{F}})}{\sqrt{\sin^2\vartheta+\cos^2\gamma\,\cos^2\vartheta}}p(\alpha'_{\text{L}}+\alpha_{\text{R}},u_{\text{F}},v_{\text{F}})$$

where α'_{L}, u_{F} and v_{F} are given by (4). Applying a 2D reconstruction (plus accounting for a possible overscan) yields the object function

$$f(x,y,z)|_{z=z(x,y)}$$

along the plane R with the correct z–position given from (2) as

$$z(x,y) = x\cos\alpha_{\mathrm{R}}\ \tan\gamma + y\sin\alpha_{\mathrm{R}}\ \tan\gamma + d\frac{\alpha_{\mathrm{R}}}{2\pi}\ .$$

The voxels have the correct x– and y–coordinates (e.g. lying on a rectangular grid in world coordinates) and the z–position $z(x,y)$, which not necessarily lies on that grid. Thus a z–interpolation step has to follow.

3.2. z–Interpolation

Before the z–interpolation can be performed a certain number of tilted images have to be reconstructed. It can be shown that using $\alpha_{\mathrm{R}} \in \Delta\alpha_{\mathrm{R}}\mathbb{Z}$ with the requirement

$$d\frac{\Delta\alpha_{\mathrm{R}}}{2\pi} + 2R_{\mathrm{M}}\tan\gamma\ \sin\tfrac{1}{2}\Delta\alpha_{\mathrm{R}} + \frac{R_{\mathrm{M}}}{R_{\mathrm{F}}}\Delta z_{\mathrm{mean}} \le S$$

imposed on the reconstruction increment $\Delta\alpha_{\mathrm{R}}$ will ensure to conserve the system's inherent resolution and thus no loss of information will occur.[12] To gain the pixel's value $f_{z_{\mathrm{R}}}(x,y)$ at the reconstruction position $z = z_{\mathrm{R}}$ we use a triangular z–filter $\Lambda(\cdot)$ of width (=half base width)

$$|d\frac{\Delta\alpha_{\mathrm{R}}}{2\pi} + 2\sqrt{x^2+y^2}\tan\gamma\ \sin\tfrac{1}{2}\Delta\alpha_{\mathrm{R}}| \vee \bar{z}$$

and the weighting equation

$$f_{z_{\mathrm{R}}}(x,y) := \left.\frac{\sum\limits_{\alpha_{\mathrm{R}}}\Lambda(z-z_{\mathrm{R}})f(x,y,z)}{\sum\limits_{\alpha_{\mathrm{R}}}\Lambda(z-z_{\mathrm{R}})}\right|_{z=z(x,y)}\ .$$

The parameter $\bar{z}$ allows to restrict the minimal filter width used and thus is a control parameter to adjust the z–resolution in the final images. Large values of $\bar{z}$ will yield large effective slice thicknesses and low image noise. All images presented below are reconstructed to achieve highest z–resolution by setting $\bar{z} = 0$.

4. RESULTS

A comprehensive comparison of all simulated table increments from $d = 1.5$ mm to $d = 96$ mm is shown in figure 2. Two transversal slices and a coronal MPR are given there. The two slices were selected so as to avoid sharp edges, such as the end of a spine, along z. This is reasonable because real patients do not have sharp edges perfectly oriented in the x–y–plane as well. (However, it will be seen later from figure 4 that slices coinciding with the edge of a vertebrae will yield severe artifacts especially for the gold standard 180°LI.) The first transaxial slice at table position $z_{\mathrm{R}} = 84$ mm (left column) represents a case where ASSR starts to show artifacts already for small cone angle whereas the second slice at $z_{\mathrm{R}} = 144$ mm does not show increasing artifacts with increasing M except for ASSR64 and ASSR96. The MPRs illustrate ASSR's performance throughout the complete volume. The high density structures depicted there are the ribs and the left and right humerus consisting of spheres with inner radius 20 mm and outer radius 25 mm. Obviously those spheres are depicted without severe artifacts for $d \le 32$ mm. Only for the two simulations with $d = 64$ mm and $d = 96$ mm artifacts become visible around the humerus. ASSR96's ribs start to show cone–beam artifacts as well.

To get a more realistic impression of how real patient images would be like when using ASSR noise has to be added to the rawdata. We have used the function `add_noise()` with `SigmaHU=8.0` as defined at the phantom page `http://www.imp.uni-erlangen.de/phantoms` to add noise corresponding to a typical thorax scan. The reconstructions of the same slices as given in figure 2 are shown in figure 3. The noise level ranges from about 10 HU in the lower thorax region to about 50 HU in the shoulder region. Obviously most of the cone–beam artifacts are occluded by the image noise. Only ASSR64 and ASSR96 show some minor artifacts emerging from the patient's ribs. Thus no disadvantages as compared to today's gold standard are to be expected when using ASSR in combination with medical cone–beam spiral CT. This even applies to future scanners with a number of detector slices significantly larger than $M = 4$.

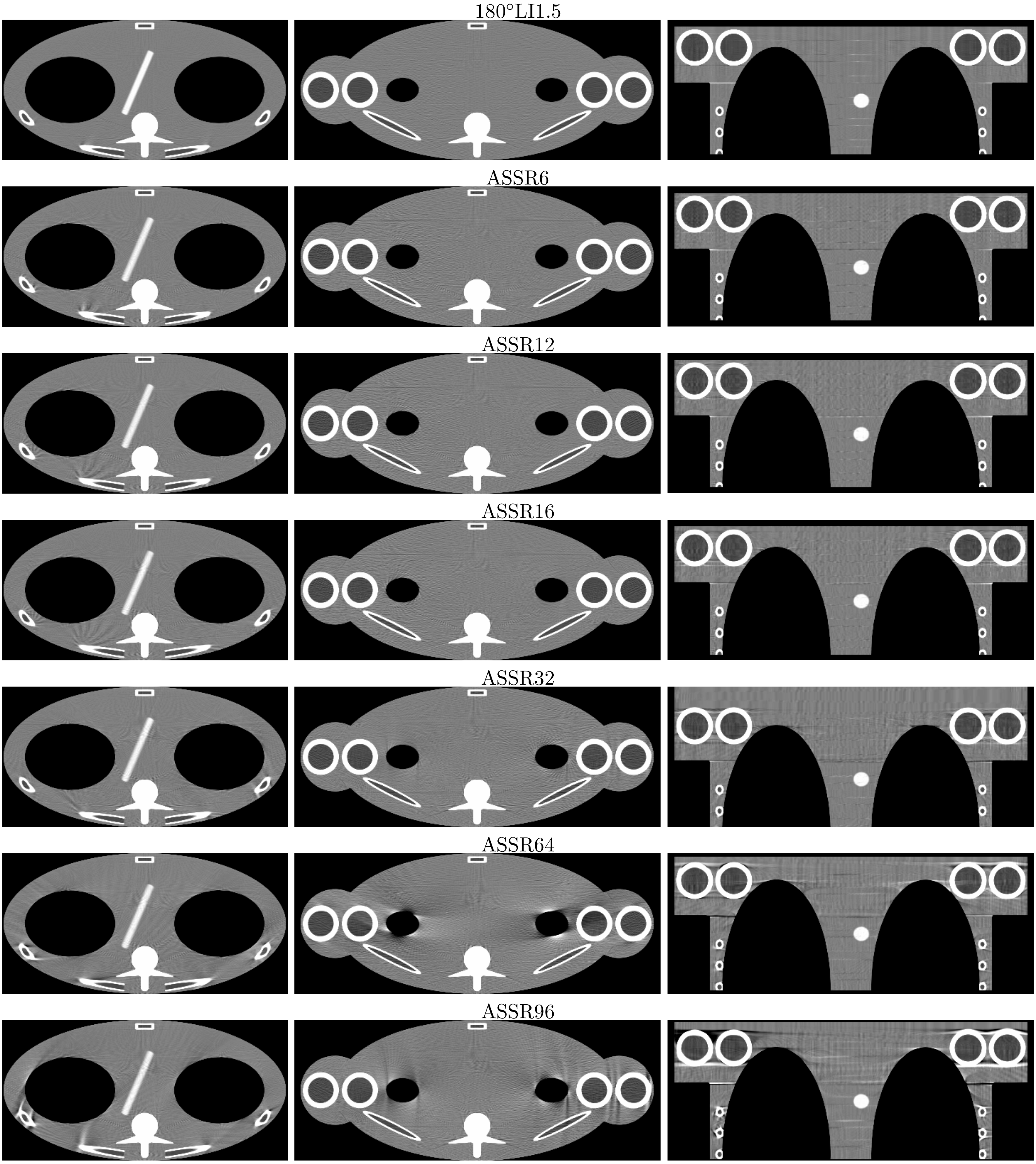

Figure 2. Comparison of all simulated scanners. Two transaxial views (z_R = 84 mm and z_R = 144 mm) and one coronal MPR are shown. The most significant differences appear in the left column where artifacts concentrate around the phantom ribs. However, except for ASSR96 these artifacts are almost negligible. Only for ASSR96, streaks emerging from the ribs become strongly apparent in the MPR as well. (0/100)

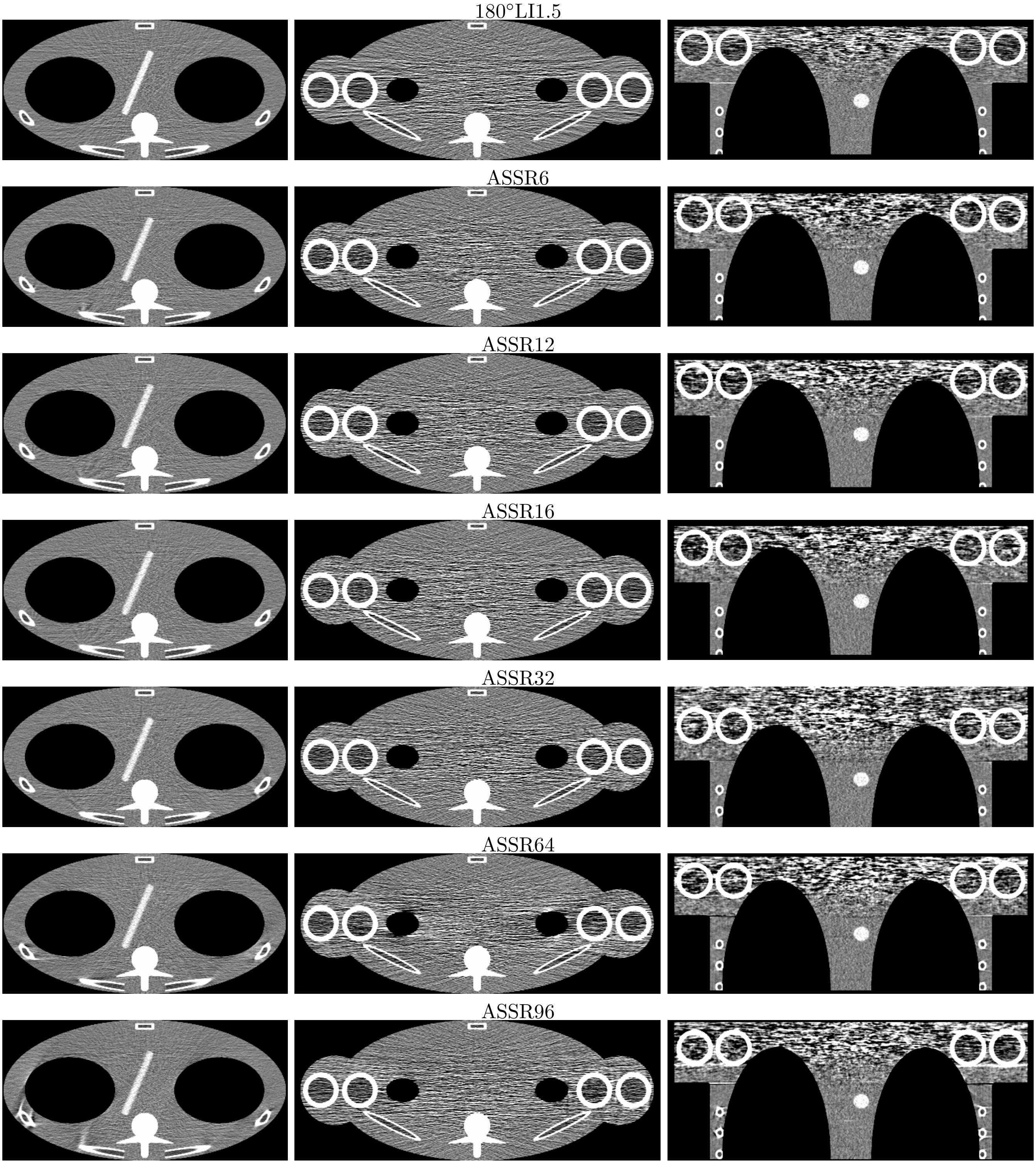

Figure 3. Comparison of all simulated scanners using additional quantum noise. The images correspond to figure 2. Except for ASSR96 the cone–beam artifacts are almost negligible. The noise levels in the center of the axial images are 10 HU (left column) and 40 HU (middle column) respectively and the noise level in the MPRs (right column) ranges from 10 HU in the lower thorax to 40 HU in the shoulder for all simulated scanners. (0/100)

We consider only those artifacts as non negligible that can be discerned under realistic, i.e. noisy, conditions. Thus, to focus attention on crucial image artifacts, we will use noisy rawdata for all images given below. Thereby, the noise simulation parameters remain the same as described above.

The improvements obtained by tilting the reconstruction slices in comparison to the original single–slice rebinning (SSR) which uses non–tilted reconstruction planes[11] are shown in figure 4 for the case $d = 64$ mm. We have used ASSR with a tilt angle of $\gamma = 0$ to obtain the SSR algorithms. Although the tilt angle is typically of the order of a few degrees only — for ASSR64 we find $\gamma = 1.24°$ — the differences between ASSR64 and SSR64 are very impressive. Since the reconstructed transversal slice was placed directly at the edge of a vertebrae the gold standard 180°LI shows severe artifacts emerging from the spine. These are not shown by ASSR since due to the large table increment only a few rays used for reconstruction are exactly parallel to the sharp edge. SSR, in contrast, shows severe artifacts of high amplitude (±100 HU) close to the vertebrae. These artifacts appear not only when reconstructing exactly at but already close to the end of a vertebrae. In addition, the display of the ribs — showing little artifacts for ASSR64 — is not acceptable for SSR64. In both, the transaxial slice and the coronal MPR the ribs seem to be a superposition of two displaced objects.

The number M of simultaneously measured slices will not increase drastically in the near future. It can be expected that $M = 8$ or $M = 12$ are quite realistic values for the next years. Thus it is of interest to compare ASSR to standard multi–slice z–interpolation algorithms as they are used on today's 4–slice machines. We use the widespread z–filtering algorithm 180°MFI for comparison.[1] The results for a typical 4–slice scanner with $d = 6$ mm and an 8–slice scanner with $d = 12$ mm are given in figure 5. It is quite surprising that ASSR shows less artifacts than 180°MFI even in the case of only 4 simultaneously measured slices. Thus ASSR might have advantages over today's standard reconstruction algorithms. Of course the same applies for the 8–slice scanner presented in subfigure 5b. However, the disadvantage of ASSR is that it does not allow to arbitrarily select the pitch value since the slice selection is intrinsically built in the ASSR algorithm. The required pitch always lies around $p = 1.5$, regardless of how many detector slices are used.[12]

5. DISCUSSION

ASSR is an efficient method for approximate cone–beam reconstruction. We have demonstrated that its image quality is comparable to standard single– or multi–slice spiral CT even for a large number of detector slices. It has been shown in a previous paper that there is no significant difference in performance between ASSR and the single–slice z–interpolation algorithm 180°LI.[12] To be more precise, ASSR typically requires two to five backprojections per slice thickness, a value that is also recommended for conventional single–slice and multi–slice spiral CT.[1] Since ASSR's reconstruction time is dominated by the backprojection step its performance is almost equivalent to the standard reconstruction algorithms available on medical CT scanners today.

For a large number of different simulated scan geometries no significant variations in ASSR's image quality have been observed. It has been shown that the algorithm's z–resolution and its image noise are comparable to the gold–standard 180°LI.[12] Since the in–plane resolution is determined by the filtered backprojection step there will be no differences as compared to conventional CT. In–plane image quality can be adjusted using appropriate reconstruction kernels as customary in medical CT.

We have demonstrated that ASSR is significantly superior to the original single–slice rebinning method. Thus the concept of tilted reconstruction planes offers great improvements to approximate cone–beam reconstruction. Moreover, it has been shown that ASSR is clearly superior to other known approximate cone–beam algorithms even for large cone angles,[13] a fact which not only applies to the achieved image quality but also to the overall performance: ASSR requires far less computational effort than other approximate algorithms. This is mainly due to the differences in 2D and 3D backprojection.

Obviously ASSR has great potential to become a practical tool for medical cone–beam reconstruction. The main disadvantage that ASSR cannot make use of overlapping data acquisition, for example to accumulate dose in order to reduce image noise, can be avoided by either selecting a slower rotation time or by increasing the tube current. This disadvantage is negligible compared to the multitude of advantages offered by ASSR: reconstruction speed, high image quality, flexibility with respect to scanner geometries and misalignments. Obviously, ASSR is a very promising candidate for future medical and non–medical cone–beam CT applications.

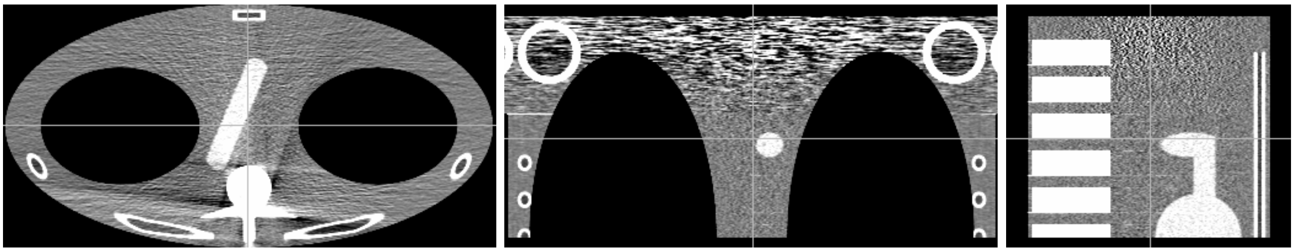

(a) 180°LI1.5

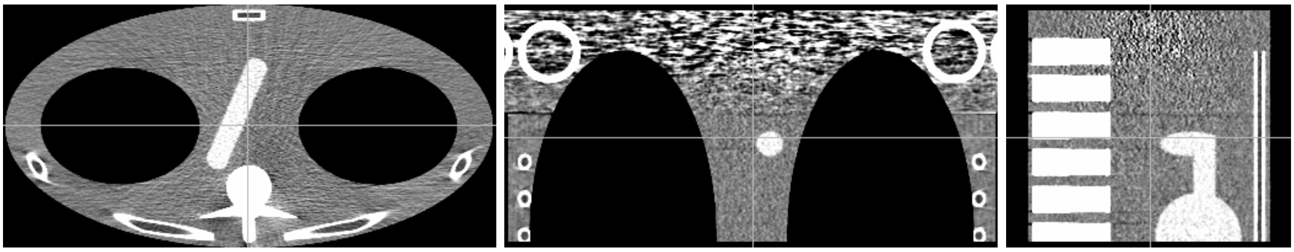

(b) ASSR64

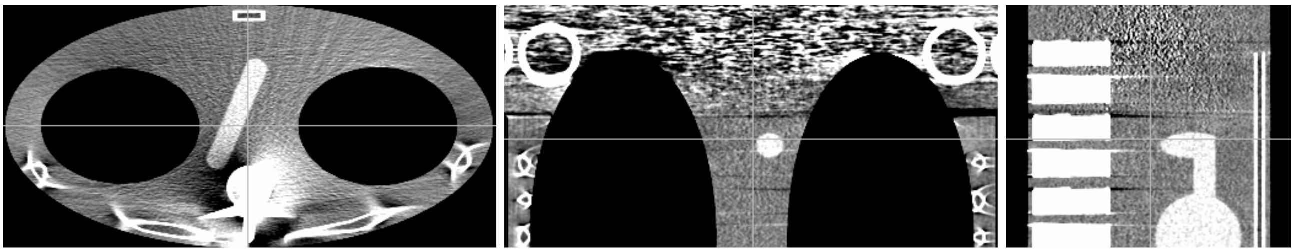

(c) SSR64

Figure 4. Comparison between the gold standard 180°LI, ASSR and the original single–slice rebinning method SSR with $d = 64$ mm, denoted here by SSR64. The transaxial slice was selected to coincide with the edge of a vertebrae. For this case 180°MLI shows significant artifacts emerging from the spine whereas ASSR64, except for the ribs, contains artifacts of minor amplitude only. As expected, the original method, SSR64, severely suffers from cone–beam artifacts due to the increased cone angle. Thus, by tilting the slices, in order to minimize data inconsistencies, great improvements in image quality are obtained. (0/100)

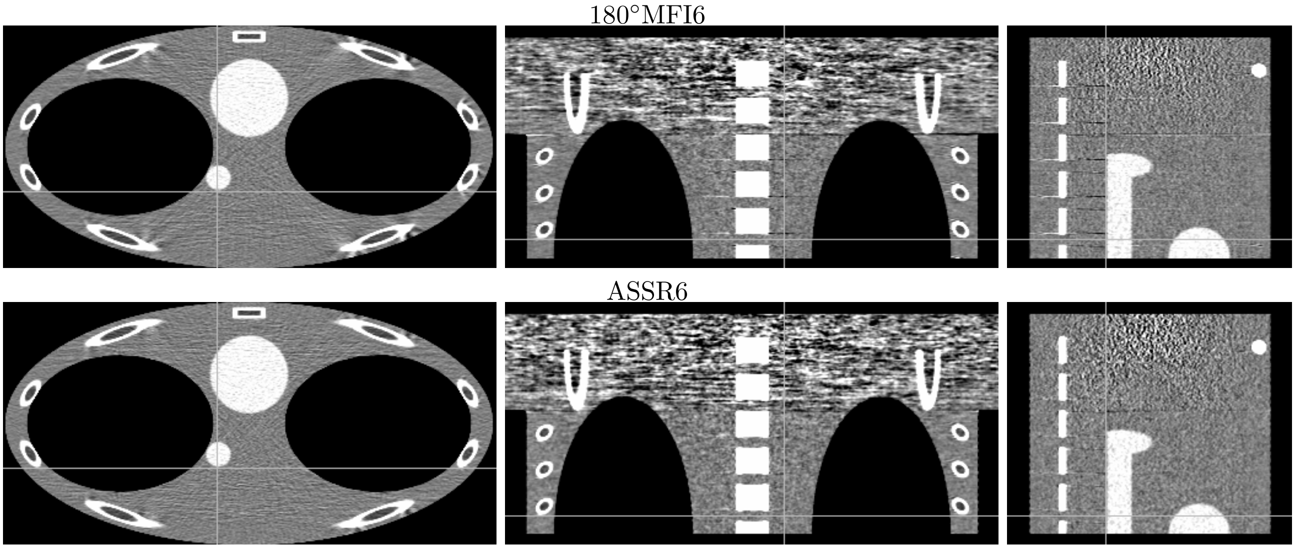

(a) $M = 4$, $d = 6$ mm, $S = 1$ mm

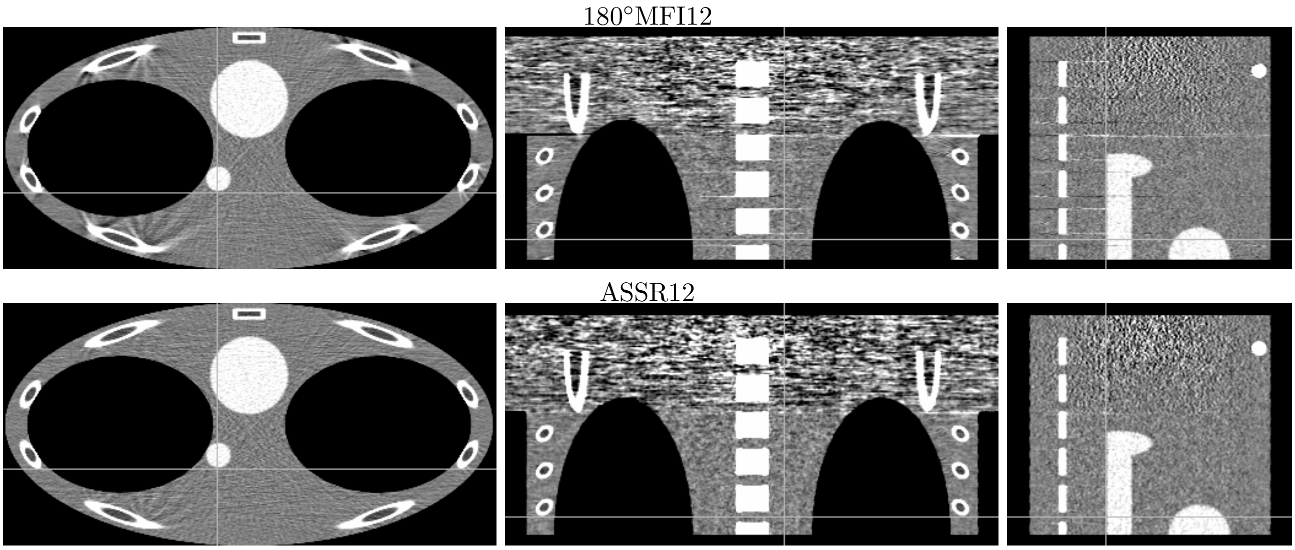

(b) $M = 8$, $d = 12$ mm, $S = 1$ mm

Figure 5. Comparison of the standard z–interpolation algorithm 180°MFI in comparison to ASSR for small cone angles. Concentrating upon the artifacts emerging from the ribs in the transversal images it becomes apparent that ASSR shows improvements as compared to the standard 180°MFI for both 4 slices (a) and 8 slices (b). The pitch was set to $p = 1.5$ for both simulations. (0/100)

ACKNOWLEDGEMENTS

This work was supported by the "FORBILD" grant AZ 286/98 "Bayerische Forschungsstiftung, München, Germany".

The CT–simulation software DRASIM was made available to us by Dr. Karl Stierstorfer, Siemens Medical Engineering, Forchheim, Germany.

We thank Dr. Theobald Fuchs for his valuable comments which have helped to improve our work.

REFERENCES

1. W. A. Kalender, *Computed Tomography*, Wiley & Sons, 2000.
2. P. Grangeat, *Analyse d'un système d'imagerie 3D par reconstruction à partir de radiographies X en géométrie conique.* PhD Thesis, Ecole Nationale Supérieure des Télécommunications (France), 1987.
3. P. Grangeat, "Mathematical framework of cone–beam 3D reconstruction via the first derivative of the radon transform," in *Mathematical Methods in Tomography*, pp. 66–97, Lecture Notes in Mathematics (Berlin: Springer), 1991.
4. H. Kudo and T. Saito, "Derivation and implementation of a cone–beam reconstruction algorithm for non–planar orbits," *IEEE Trans. Med. Imag.* **MI–13**, pp. 196–211, 1994.
5. M. Defrise and R. Clack, "A cone–beam reconstruction algorithm using shift variant filtering and cone–beam backprojection," *IEEE Trans. Med. Imag.* **MI–13**, pp. 186–195, 1994.
6. L. Feldkamp, L. Davis, and J. Kress, "Practical cone–beam algorithm," *Journal of the Optical Society of America* **1**, pp. 612–619, June 1984.
7. X. Yan and R. Leahy, "Cone–beam tomography with circular, elliptical and spiral orbits," *Phys. Med. Biol.* **37**, pp. 493–506, 1992.
8. G. Wang, T. Lin, P. Cheng, and D. Shinozaki, "A general cone–beam reconstruction algorithm," *IEEE Trans. Med. Imag.* **MI–12**, pp. 486–496, 1993.
9. S. Schaller, T. Flohr, and P. Steffen, "New, efficient Fourier–reconstruction method for approximate image reconstruction in spiral cone–beam CT at small cone–angles," *SPIE Medical Imaging Conference Proc.* **3032**, pp. 213–224, 1997.
10. P. Danielsson, P. Edholm, J. Eriksson, M. Magnusson Seger, and H. Turbell, "The original PI–method for helical cone–beam CT," *Proc. of the 1999 Int. Meeting on Fully 3D Image Reconstruction* , pp. 3–6, June 1999.
11. F. Noo, M. Defrise, and R. Clackdoyle, "Single–slice rebinning method for helical cone–beam CT," *Phys. Med. Biol.* **44**, pp. 561–570, 1999.
12. M. Kachelrieß, S. Schaller, and W. A. Kalender, "Advanced single–slice rebinning in cone–beam spiral CT," *Med. Phys.* **27**, pp. 754–772, Apr. 2000.
13. H. Bruder, M. Kachelrieß, S. Schaller, and T. Mertelmeier, "Performance of approximate cone–beam reconstruction in multislice computed tomography," *SPIE Medical Imaging Conference Proc.* **3979**, pp. 541–555, 2000.